

Optically-excited acoustic waves in Si nanowires probed by time-resolved HOLZ lines

He Wang(王贺), Shuaishuai Sun(孙帅帅), Yizhe Wang(王怡哲), Qianming An(安乾明), Xianhui Ye(叶显珲), Jun Li(李俊), Huanfang Tian(田焕芳), Huaixin Yang(杨槐馨), Jianqi Li(李建奇), and Zian Li(李子安)
Citatio: Chin. Phys. B, 2025, 34 (**9**): 098701. DOI: 10.1088/1674-1056/ade250
http://cpb.iphy.ac.cn; http://iopscience.iop.org/cpb

What follows is a list of articles you may be interested in

A large language model-powered literature review for high-angle annular dark field imaging

Wenhao Yuan(袁文浩), Cheng Peng(彭程), and Qian He(何迁)
Chin. Phys. B, 2024, 33 (**9**): 098703. DOI: 10.1088/1674-1056/ad625c

Subtraction of liposome signals in cryo-EM structural determination of protein-liposome complexes

Shouqing Li(李首卿), Ming Li(李明), Yumei Wang(王玉梅), and Xueming Li(李雪明)
Chin. Phys. B, 2024, 33 (**8**): 088702. DOI: 10.1088/1674-1056/ad4cdb

Structural biology revolution led by technical breakthroughs in cryo-electron microscopy

Chang-Cheng Yin(尹长城)
Chin. Phys. B, 2018, 27 (**5**): 058703. DOI: 10.1088/1674-1056/27/5/058703

Bio-macromolecular dynamic structures and functions, illustrated with DNA, antibody, and lipoprotein

Lu Gou(缑璐), Taoli Jin(金桃丽), Shuyu Chen(陈淑玉), Na Li(李娜), Dongxiao Hao(郝东晓), Shengli Zhang(张胜利), Lei Zhang(张磊)
Chin. Phys. B, 2018, 27 (**2**): 028708. DOI: 10.1088/1674-1056/27/2/028708

Lipoprotein in cholesterol transport: Highlights and recent insights into its structural basis and functional mechanism

Shu-Yu Chen(陈淑玉), Na Li(李娜), Tao-Li Jin(金桃丽), Lu Gou(缑璐), Dong-Xiao Hao(郝东晓), Zhi-Qi Tian(田芷淇), Sheng-Li Zhang(张胜利), Lei Zhang(张磊)
Chin. Phys. B, 2018, 27 (**2**): 028702. DOI: 10.1088/1674-1056/27/2/028702

RAPID COMMUNICATION

Optically-excited acoustic waves in Si nanowires probed by time-resolved HOLZ lines

He Wang(王贺)[1], Shuaishuai Sun(孙帅帅)[2], Yizhe Wang(王怡哲)[1], Qianming An(安乾明)[1], Xianhui Ye(叶显珲)[1], Jun Li(李俊)[2], Huanfang Tian(田焕芳)[2], Huaixin Yang(杨槐馨)[2], Jianqi Li(李建奇)[2,†], and Zian Li(李子安)[1,‡]

[1] *School of Physical Science and Technology, Guangxi University, Nanning* 530004, *China*
[2] *Institute of Physics, Chinese Academy of Sciences, Beijing* 100190, *China*

(Received 10 May 2025; revised manuscript received 6 June 2025; accepted manuscript online 9 June 2025)

Exploring advanced techniques capable of probing nanometric acoustic waves in nanostructures is critically important for the development of miniaturized acoustic devices. In this study, we probe the optically-excited acoustic waves in a single silicon nanowire (NW) using the time-resolved (tr-) high-order Laue-zone (HOLZ) lines under convergent-beam electron diffraction (CBED) conditions in an ultrafast transmission electron microscope (UTEM). We devise an experimental scheme to obtain tr-HOLZ lines under off-zone-axis CBED conditions. We also propose a geometric description of HOLZ line formation and use this alternative description to quantitatively evaluate the dynamics of optically-excited silicon NW. Using part of the deformation gradient tensor, our simulations of the dynamics of Si NW reproduce the experimental results. We further discuss the feasibility of a full retrieval of the deformation gradient tensor by using a set of HOLZ lines from three zone axes. Our findings illustrate a strategy for the quantitative access to dynamical acoustic waves optically excited in micro- and nano-structures using UTEM.

Keywords: ultrafast transmission electron microscope, high-order Laue-zone lines, pulsed laser excitation, acoustic waves

PACS: 87.64.Ee, 61.05.jm

DOI: 10.1088/1674-1056/ade250 **CSTR:** 32038.14.CPB.ade250

1. Introduction

Ultrafast transmission electron microscopy (UTEM) techniques have been applied to structural and electronic dynamics, such as structural phase transitions,[1,2] acoustic wave propagation,[3–6] dielectric response,[7–9] and spin dynamics[10] in various materials. Previous UTEM experiments employed bright-field imaging[4,11–13] and electron diffraction[3,5,14,15] to elucidate acoustic responses. Compared to other conventional electron microscopy techniques, including bright-field imaging and selected-area electron diffraction, the high-order Laue-zone (HOLZ) lines in convergent-beam electron diffraction (CBED) patterns are more sensitive to small lattice deformations (spatial resolution 1 nm, sensitivity 10^{-4}).[16–18] Recent studies have used HOLZ lines in CBED to quantitatively analyze the propagation of strain waves in nanomaterials.[19–24] Most existing methodologies rely on single-axis CBED data in conjunction with dynamical simulations to achieve accurate measurements of lattice deformation. However, previous studies have revealed that CBED patterns acquired along a single zone axis may exhibit intrinsic ambiguities, as different real-space lattice deformations can produce indistinguishable diffraction patterns. Although various approaches have been employed to investigate this phenomenon, the reported findings remain inconsistent,[25,26] indicating that the underlying causes of the ambiguity and the sensitivity of higher-order Laue-zone (HOLZ) lines to components of the deformation gradient tensor are not yet fully understood.

In this study, we used UTEM to optically excite acoustic waves in individual silicon nanowires (NWs) and subsequently recorded higher-order Laue-zone (HOLZ) lines under CBED conditions. To illustrate the inherent ambiguity of the CBED method, we simulated HOLZ patterns using two different deformation gradient tensors, which yielded nearly indistinguishable diffraction patterns. To clarify the origin of this effect, we introduce a geometric model describing HOLZ line formation and apply this framework to quantitatively analyze the acoustic wave dynamics in Si NWs. Finally, we explore the feasibility of fully reconstructing the deformation gradient tensor from HOLZ line data.

2. Experimental details

UTEM experiments were conducted at the Synergetic Extreme Condition User Facility (SECUF, Beijing, China). The

†Corresponding author. E-mail: LJQ@iphy.ac.cn
‡Corresponding author. E-mail: zianli@gxu.edu.cn

© 2025 Chinese Physical Society and IOP Publishing Ltd. All rights, including for text and data mining, AI training, and similar technologies, are reserved.

UTEM is a transmission electron microscope (TEM) (JEM-2100plus, JEOL Inc.) retrofitted with a femtosecond (fs) laser (Spectra-Physics, Spirit 1040) and a nanosecond (ns) laser (ZYLaser, Stele-A-1). The sample was pumped by a pulsed laser (pulse width 300 fs, wavelength 520 nm). Part of the fs laser pulses were used to trigger the ns laser via a photodiode and a digital delay generator (SRS, DG645). The 15-μm-tip LaB_6 photocathode was illuminated by the pulsed laser (10 ns, $\lambda = 355$ nm) to generate photoelectrons. The pulsed electron beam was focused to 200 nm with a semi-convergence angle of 15 mrad to form the convergent-beam electron diffraction (CBED) pattern. Each electron pulse that reached the sample contained approximately 10^5 electrons. The time resolution of the ns stroboscopic UTEM was estimated to be around 10 ns (FWHM), limited by the pulse duration of the 355 nm laser. Each time-resolved CBED pattern was acquired using a fiber-coupled CMOS camera (OneView, Gatan Inc.) with an exposure time of 2 seconds. The delay time was adjusted using the digital delay generator. The repetition rates for both the fs and ns lasers were set to 10 kHz (see supplementary material 1 for details).

3. Results

3.1. Time-resolved CBED and off-zone-axis HOLZ lines

Figure 1(a) shows a schematic representation of the tr-CBED experimental setup, with the Si NW having one end fixed as a nano-cantilever. Figure 1(b) shows the Si NW (6.18 μm in length, 220 nm in diameter), suspended on a 2000-mesh Cu grid. Figure 1(c) shows a [112]-oriented SAED pattern taken from the area circled in Fig. 1(b), revealing that the long axis of the Si NW corresponds to the ⟨111⟩ crystallographic direction. For better visibility of the HOLZ lines, the Si NW was tilted away from the initial [112] zone axis (for details, see supplementary material 2). In the tr-CBED experiment, we used a pulsed laser ($\lambda = 520$ nm) to optically excite the Si NW, and the resultant thermal stress initiated acoustic waves that propagated through it. We stroboscopically recorded off-zone-axis CBED patterns locally from the Si NW using convergent (semi-convergence angle $\alpha = 15$ mrad) pulsed photoelectrons at varying delay times (Δt). Figure 1(d) shows a typical off-zone-axis CBED pattern, where all HOLZ lines are well indexed by Miller indices.

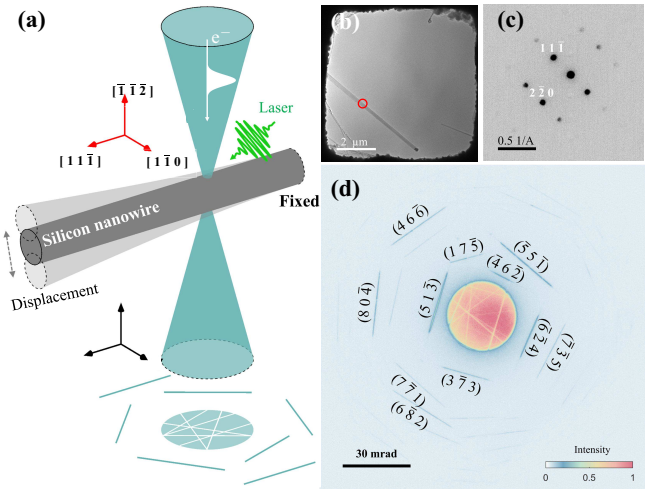


Fig. 1. An optically excited Si NW probed by time-resolved (tr-) HOLZ lines under CBED conditions. (a) Schematic representation of the experimental setup with the microscope XYZ coordinate system and the Miller indices lattice coordinate system. (b) Bright-field TEM image of the Si NW with one end fixed on the Cu grid. The red circle denotes the area for HOLZ line recording. (c) Selected area electron diffraction pattern taken along the [112] zone-axis. (d) Off-zone-axis CBED pattern taken along a direction deviating from the exact [112] zone-axis, for better visibility of the HOLZ lines.

3.2. Optically excited acoustic waves in Si NW probed by HOLZ excess lines

To analyze the transient changes in the HOLZ lines, we select a rectangular area around them and integrate the intensity along the line direction.[22,23] Figures 2(a) and 2(c) display the HOLZ line profiles (integrated intensity in pseudo-color) for $(\bar{5}\ 5\ \bar{1})$ over the −200 ns to 5000 ns timescale and for all selected HOLZ lines between 30000 ns and 34000 ns, respectively. In the time range from −200 ns to 5000 ns, the HOLZ lines exhibit complex oscillations that gradually diminish over time (Fig. 2(a)), which can be attributed to the dramatic lattice deformation initiated by the pulsed laser.[4,27] Once the time delay reaches 30000 ns and beyond, the oscillation amplitude of each HOLZ line reduces to below 2 mrad, and the acoustic oscillations simplify to fundamental and a few high-order modes of a typical nano-cantilever, as shown in Fig. 2(c) with a time range from 30000 ns to 34000 ns in 10 ns time steps (see supplementary material video 1 and video 2).

To better visualize the dynamics of the HOLZ line profiles, we further extract the change in the HOLZ excess line G_E by using the line-intensity profiles (Fig. 2(c)). Figure 3(a) shows the evolution of all HOLZ lines as a function of time delay. To demonstrate the ambiguity inherent in the CBED method, we perform simulations of the dynamic displacement of HOLZ excess lines as acoustic waves propagate through the Si NW on the ns time scale. The details of the simulations are given in supplementary material 3. Figures 3(b) and 3(c) show the simulated evolution of the corresponding HOLZ lines using two different estimated deformation gradient tensors F from Figs. 3(d) and 3(e). Notably, both simulation 1 and simulation 2 in Fig. 3 accurately reproduce the experimental results, demonstrating excellent agreement in both the oscillatory amplitude and frequency for all observed HOLZ excess lines. Thus, we observe that for a given incident zone-axis, not all the nine terms in F will lead to measurable shifts of HOLZ excess lines.[28,29] We discuss this cause-and-effect relationship using a geometric description of HOLZ line formation below.

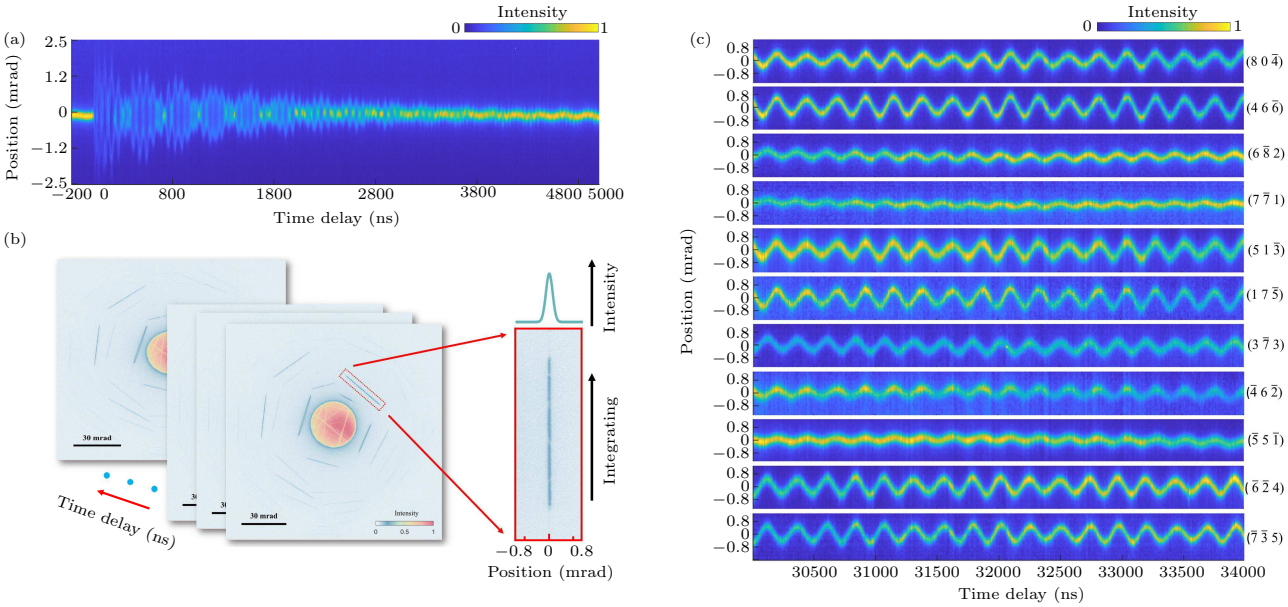


Fig. 2. Time-resolved (tr-) HOLZ-line profiles extracted from tr-CBED patterns. (a) Time-dependent $(\bar{5}\ 5\ \bar{1})$ HOLZ line profiles in the time range from −200 ns to 5000 ns with a time step of 10 ns. (b) HOLZ line profile extracted from a single HOLZ line at a specific time snapshot. (c) All Miller indices tr-HOLZ line profiles in the time range from 30000 ns to 34000 ns with a time step of 10 ns.

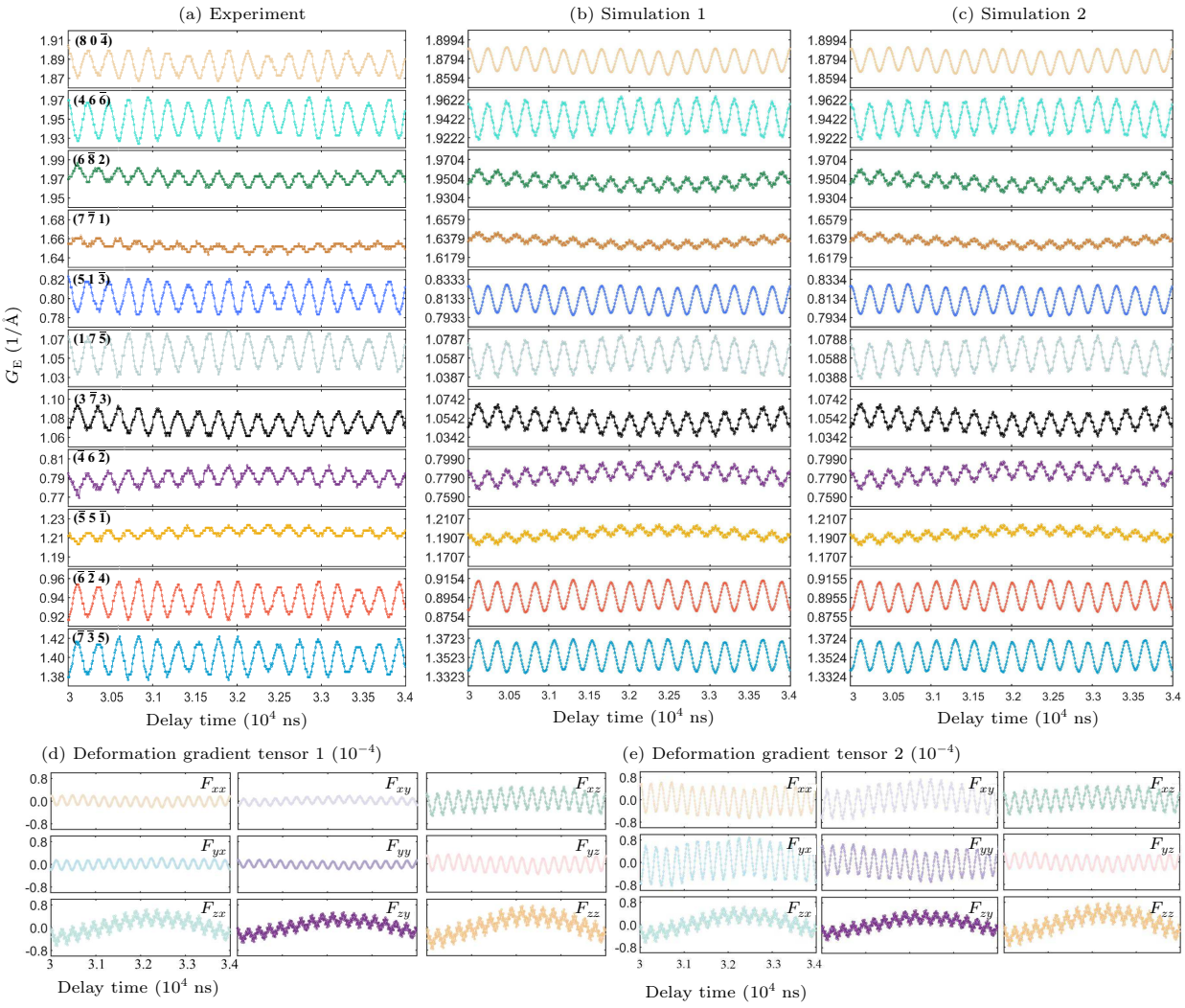


Fig. 3. Comparative experiments and simulations on the time-dependent variation of HOLZ excess line distance G_E. (a) Experimental tr-HOLZ excess line distances G_E. (b) Simulation 1 of tr-HOLZ excess line G_E and (d) the corresponding deformation gradient tensor F. (c) Simulation 2 of G_E and (e) the corresponding F. Note that only F_{xx}, F_{xy}, F_{yx}, and F_{yy} differ between the two simulations.

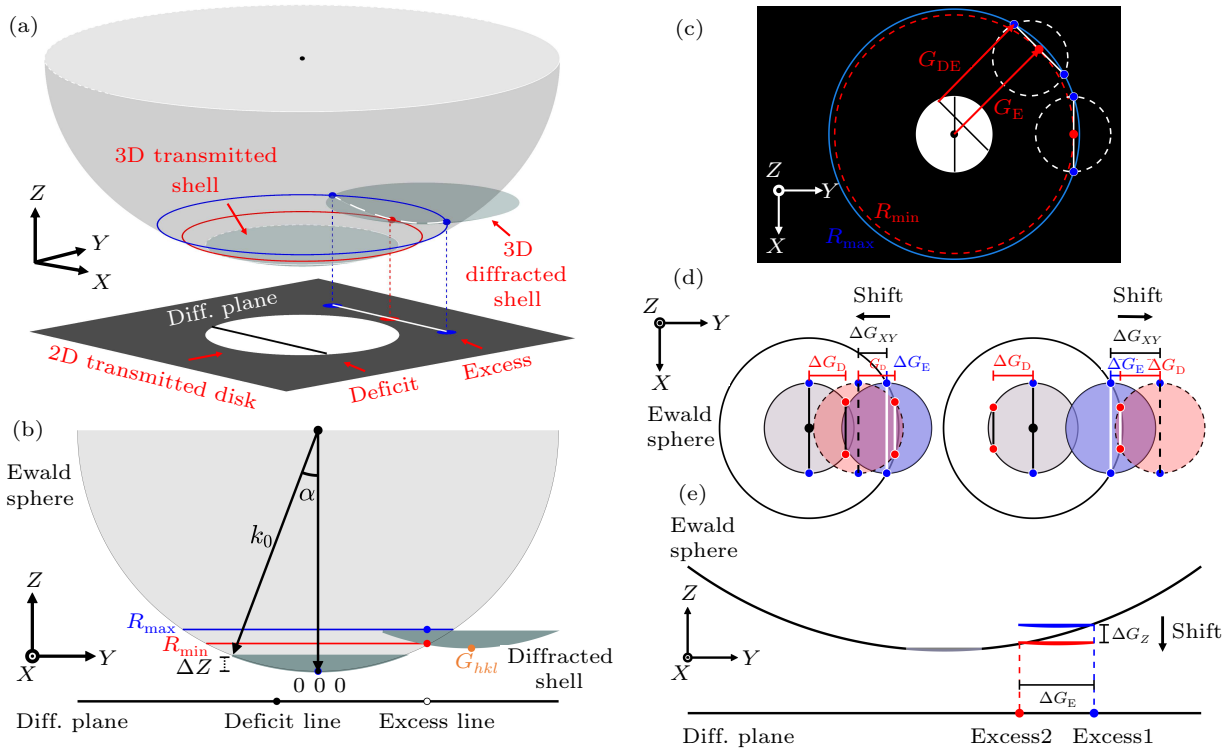


Fig. 4. Geometric description of HOLZ line formation and sensitivity with respect to lattice deformation. (a) Perspective view of HOLZ lines under CBED conditions. (b) Side view, showing the electron wave vector k_0, the height of transmitted and diffracted shells ΔZ, the semi-convergence angle α, and the respective maximum and minimum radii $R_{\max}$ and $R_{\min}$ at which the diffracted shell intersects the Ewald sphere. (c) Top view, where the blue and red points indicate the intersections between the Ewald sphere and diffracted shell at $R_{\max}$ and $R_{\min}$, respectively. G_{DE} is the distance between the excess-deficit line pair, and G_{E} is the excess-center line distance. (d) The effect of lateral (X, Y) movement of the diffracted disk on the lateral (X, Y) shift of HOLZ lines. The transmitted disk, the original diffracted disk, and the shifted diffracted disk (dashed line) are denoted. The line segments denoted by ΔG_{D} and ΔG_{E} represent the changes in G_{D} and G_{E}, and ΔG_{XY} is the distance change between the initial and shifted diffracted disks. (e) The effect of vertical (Z-axis) movement of the diffracted shell on the lateral (X, Y) shift of HOLZ lines.

Figures 4(a)–4(c) illustrate a schematic representation of HOLZ line formation under CBED conditions, showing the side and top views of the scattering geometry, respectively. In this framework, we use a static Ewald sphere model, where the Ewald sphere remains fixed in the XYZ reciprocal coordinate system, while the incident electron wavevectors (k_0) and the crystal lattice are tilted. Under CBED conditions with a semi-convergence angle α, the incident k_0 at varying angles corresponds to distinct layers of the Ewald sphere, leading to the formation of a transmitted shell with a height difference ΔZ between k_0 at α and at 0° (Fig. 4(b)). For a 200 kV incident electron beam ($k_0 = 39.84$ Å^{-1}) and a semi-convergence angle of 15 mrad, ΔZ is approximately 0.005 Å^{-1}.

Similarly, the diffracted shell $(h\,k\,l)$ is linked to the transmitted shell by the reciprocal lattice vector G_{hkl} and remains parallel to it.[30] The excess HOLZ lines arise from the two-dimensional projection of the three-dimensional intersection between the diffracted shells and the Ewald sphere onto the diffraction plane (Fig. 4(a)). These lines can be approximated as the connection between the two intersection points (blue) on the uppermost layer of the diffracted shell, as indicated by the white lines in Fig. 4(c). Here, G_{D} and G_{E} denote the distances from the transmitted disk center to the deficit and excess lines, respectively, while G_{DE} represents the separation between the deficit-excess line pair (see supplementary material 4 for details).

Since a real-space displacement Δr corresponds to a reciprocal-space shift Δg that manifests as positional changes in diffracted spots and disks, we analyze the influence of lattice deformation on the lateral (X, Y) displacement of HOLZ lines. As illustrated in Fig. 4(d), the excess and deficit HOLZ lines shift as the diffracted disk (initially blue) moves along the $-Y$ and $+Y$ directions to its new positions (shifted red), leading to changes in the diffracted disk position ΔG_{XY}, the excess line ΔG_{E}, and the deficit line ΔG_{D}. Crucially, the following relationships hold:

$$\Delta G_{XY} = \Delta G_{\mathrm{D}} - \Delta G_{\mathrm{E}}, \quad \text{(for displacement along } -Y\text{)},$$
$$\Delta G_{XY} = \Delta G_{\mathrm{D}} + \Delta G_{\mathrm{E}}, \quad \text{(for displacement along } +Y\text{)}.$$

These equations demonstrate that the lateral shift ΔG_{XY} of the diffracted disk induces nearly equivalent changes in the HOLZ lines (ΔG_{D} and ΔG_{E}).

However, the shift of diffraction disks caused by elastic lattice deformation is usually minimal. For instance, our simulations show that the displacement of the diffraction shell in reciprocal space does not exceed 0.002 Å^{-1}. Under the

current experimental conditions (200 kV, 4k resolution), each pixel corresponds to approximately 0.0014 Å^{-1}, meaning the HOLZ line shift induced by ΔG_{XY} is only about 2 pixels. Therefore, the HOLZ line displacement due to ΔG_{XY} can be neglected. In contrast, even a minor vertical shift (ΔG_Z) along the Z-axis can produce substantial lateral displacements (ΔG_{E}, ΔG_{D}) in the HOLZ lines. As depicted in Fig. 4(e), a small vertical displacement ΔG_Z of the diffracted disk (from blue to red) results in a pronounced lateral shift ΔG_{E} in the excess HOLZ line. This amplification arises from the curvature of the Ewald sphere, which magnifies small Z-axis variations into significant XY-plane displacements. Therefore, single-zone-axis CBED reveals only Z-direction changes in diffraction shells. Complete 3D characterization requires multi-zone-axis data. Our geometric framework analysis independently reproduces Morawiec's conclusions.[26]

3.3. Retrieval of deformation gradient tensor F via HOLZ lines from three zone-axis CBED patterns

To retrieve the full deformation gradient tensor via HOLZ lines from three off-zone-axis CBED patterns, we first define two Cartesian coordinate systems: the microscope XYZ in Fig. 5(a) and the reciprocal lattice xyz in Fig. 5(b). The initial reciprocal basis vectors are a_0^*, b_0^*, c_0^*, and the deformed ones are a^*, b^*, c^*. Figure 5(c) shows the projected basis vectors along the Z axis at three different zone axes for the same deformed lattice. The center (G_X, G_Y, G_Z) of the diffracted shell G_{hkl} in the microscope XYZ Cartesian coordinate system is given by

$$\begin{pmatrix} G_X \\ G_Y \\ G_Z \end{pmatrix} = \boldsymbol{A}^* \begin{pmatrix} h \\ k \\ l \end{pmatrix}, \quad \boldsymbol{A}^* = \begin{pmatrix} a_X^* & b_X^* & c_X^* \\ a_Y^* & b_Y^* & c_Y^* \\ a_Z^* & b_Z^* & c_Z^* \end{pmatrix}_{XYZ}, \tag{1}$$

where the matrix $\boldsymbol{A}^*$ represents the reciprocal basis vectors a^*, b^*, c^* in the microscope XYZ coordinate system.

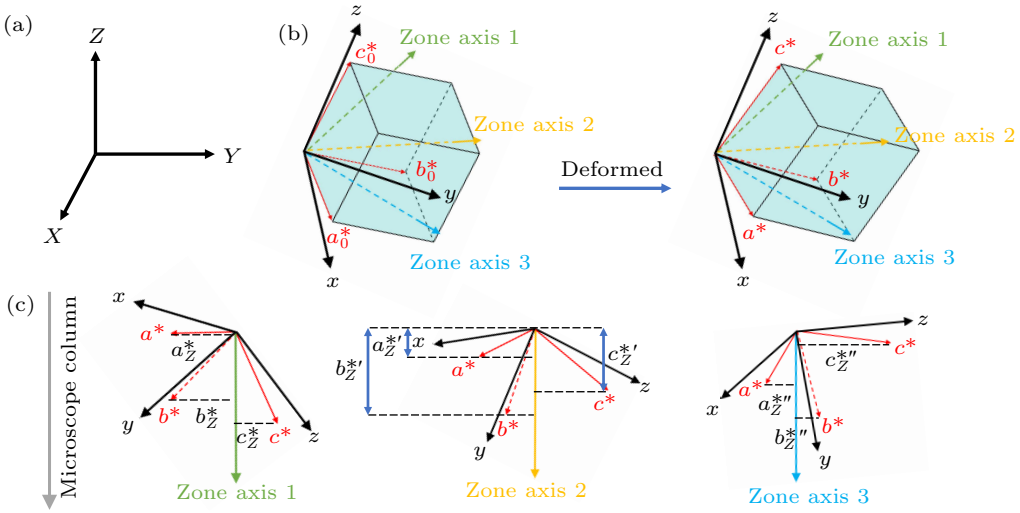


Fig. 5. Reconstruction of 3D lattice deformation with HOLZ line measurements along three independent zone axes. (a) The microscope XYZ Cartesian coordinate system. (b) The reciprocal lattice xyz Cartesian coordinate system with the initial and deformed lattices. The vectors (a_0^*, b_0^*, c_0^*) and (a^*, b^*, c^*) represent the initial and deformed bases, respectively, which are defined in the xyz Cartesian coordinate system. (c) Projections of the reciprocal basis onto the Z-axis (along the microscope column direction) of the XYZ coordinate system for three different zone axes.

As discussed in Fig. 4, the vertical shift ΔG_Z can be accurately measured by the change in the HOLZ excess lines ΔG_{E} (for details, see the supplementary material 5). For a given zone-axis, the Z-component $(a_Z^*(t), b_Z^*(t), c_Z^*(t))$ of the basis vectors $(a^*(t), b^*(t), c^*(t))$ can be obtained by measuring $G_{Z1}(t)$, $G_{Z2}(t)$, and $G_{Z3}(t)$ of three diffracted shells at different delay times as

$$\begin{pmatrix} a_Z^*(t) \\ b_Z^*(t) \\ c_Z^*(t) \end{pmatrix} = \begin{pmatrix} h_1 & k_1 & l_1 \\ h_2 & k_2 & l_2 \\ h_3 & k_3 & l_3 \end{pmatrix}^{-1} \begin{pmatrix} G_{Z1}(t) \\ G_{Z2}(t) \\ G_{Z3}(t) \end{pmatrix}. \tag{2}$$

In the other two zone axes, the Z components of the basis vectors for the corresponding zone axes at different delay times $(a_Z^*(t)', b_Z^*(t)', c_Z^*(t)')$ and $(a_Z^*(t)'', b_Z^*(t)'', c_Z^*(t)'')$ are given below:

$$\begin{pmatrix} a_Z^*(t)' \\ b_Z^*(t)' \\ c_Z^*(t)' \end{pmatrix} = \begin{pmatrix} h_1' & k_1' & l_1' \\ h_2' & k_2' & l_2' \\ h_3' & k_3' & l_3' \end{pmatrix}^{-1} \begin{pmatrix} G_{Z1}(t)' \\ G_{Z2}(t)' \\ G_{Z3}(t)' \end{pmatrix}, \tag{3}$$

$$\begin{pmatrix} a_Z^*(t)'' \\ b_Z^*(t)'' \\ c_Z^*(t)'' \end{pmatrix} = \begin{pmatrix} h_1'' & k_1'' & l_1'' \\ h_2'' & k_2'' & l_2'' \\ h_3'' & k_3'' & l_3'' \end{pmatrix}^{-1} \begin{pmatrix} G_{Z1}(t)'' \\ G_{Z2}(t)'' \\ G_{Z3}(t)'' \end{pmatrix}, \tag{4}$$

with the geometric relationship between the XYZ- and the xyz-coordinates, the deformed reciprocal lattice $\boldsymbol{A}_{xyz}^*$ and the projection matrix $\boldsymbol{Z}$ satisfy the following equations:

$$\boldsymbol{W} \times \boldsymbol{A}_{xyz}^* = \boldsymbol{Z}_{XYZ}^*, \tag{5}$$

$$\boldsymbol{W} = \begin{pmatrix} w_x & w_y & w_z \\ w_x' & w_y' & w_z' \\ w_x'' & w_y'' & w_z'' \end{pmatrix}, \tag{6}$$

$$\boldsymbol{A}^*_{xyz} = \begin{pmatrix} a_x^*(t) & b_x^*(t) & c_x^*(t) \\ a_y^*(t) & b_y^*(t) & c_y^*(t) \\ a_z^*(t) & b_z^*(t) & c_z^*(t) \end{pmatrix}_{xyz}, \tag{7}$$

$$\boldsymbol{Z}^*_{XYZ} = \begin{pmatrix} a_Z^*(t) & b_Z^*(t) & c_Z^*(t) \\ a_Z^*(t)' & b_Z^*(t)' & c_Z^*(t)' \\ a_Z^*(t)'' & b_Z^*(t)'' & c_Z^*(t)'' \end{pmatrix}_{XYZ}, \tag{8}$$

where $\boldsymbol{W}$ is the weight matrix, which can be obtained by the angles between the xyz axes and the Z axis at different zone axes. Since the reciprocal space lattice corresponds to the real-space lattice, once the $\boldsymbol{A}^*_{xyz}$ matrix is determined, the real-space lattice can also be determined.

Previously, acquiring CBED patterns from three independent zone axes at the same sample location was experimentally challenging. The development of the rotation holder significantly improved this process by enabling in-plane sample rotation and large-angle tilting, thereby facilitating the collection of three distinct zone-axis CBED patterns. Furthermore, recent advancements in TEM instrumentation, including optimized pulse-driven field-emission photocathodes,[31–33] direct-detection cameras[34], and automated tilt-control systems,[35] have further enhanced experimental efficiency, making three-zone-axis CBED measurements more accessible.

4. Conclusion

In summary, we optically excited acoustic waves in a single silicon NW and monitored the resulting elastic deformation using tr-HOLZ lines under CBED conditions in a UTEM. To enhance the visibility of HOLZ lines, we developed an experimental approach involving CBED pattern acquisition under off-zone-axis conditions.

We employed a geometric model of HOLZ line formation to quantitatively assess the elastic deformations in the Si NW, enabling partial determination of the deformation gradient tensor. Simulations based on the derived tensor components showed excellent agreement with experimental observations. However, we identified inherent ambiguities in the CBED-based HOLZ line method for precise determination of the full deformation gradient tensor. We analyzed the origin of these ambiguities and propose a solution involving the use of HOLZ line datasets from three distinct zone axes to enable complete tensor retrieval.

This study presents a reliable method for analyzing acoustic wave propagation in nanostructures with spatial precision, utilizing HOLZ line analysis in CBED mode within a UTEM system. The developed technique enables nanoscale strain mapping with unprecedented spatiotemporal resolution, offering new avenues for advanced materials characterization.

Acknowledgments

This project is supported by the Guangxi Natural Science Foundation (Grant No. 2024GXNSFDA010014), the National Natural Science Foundation of China (Grant Nos. 12364018 and U22A6005), the Guangxi Science and Technology Major Program (Grant No. AA23073019), and the Innovation Project of Guangxi Graduate Education (Grant Nos. YCBZ2022049 and YCBZ2023015). This work is also supported by the Synergetic Extreme Condition User Facility (SECUF, https://cstr.cn/31123.02.SECUF). The Center for Instrumental Analysis of Guangxi University is acknowledged for providing research facilities and resources for the experiments.

References

[1] Zhang M, Li Z A, Tian H, Yang H and Li J 2018 *Appl. Phys. Lett.* **113** 133103
[2] Danz T, Domröse T and Ropers C 2021 *Science* **371** 371
[3] Harb M, Peng W, Sciaini G, Hebeisen C T, Ernstorfer R, Eriksson M A, Lagally M G, Kruglik S G and Miller R J D 2009 *Phys. Rev. B* **79** 094301
[4] McKenna A J, Eliason J K and Flannigan D J 2017 *Nano Lett.* **17** 3952
[5] Zhang Y, Sun S, Wang W, Tian H, Li J, Li J and Yang H 2023 *Phys. Rev. B* **108** 245426
[6] Qian Q, Shen X, Luo D, Jia L, Kozina M, Li R, Lin M F, Reid A H, Weathersby S, Park S, Yang J, Zhou Y, Zhang K, Wang X and Huang S 2020 *ACS Nano* **14** 8449
[7] Fu X, Barantani F, Gargiulo S, Madan I, Berruto G, LaGrange T, Jin L, Wu J, Vanacore G M, Carbone F and Zhu Y 2020 *Nat. Commun.* **11** 5770
[8] Plemmons D A, Suri P K and Flannigan D J 2015 *Chem. Mater.* **27** 3178
[9] Lian Y, Sun J and Jiang L 2023 *Int. J. Mech. Syst. Dyn.* **3** 192
[10] Zhou F, Liu H, Zajac M, Hwangbo K, Jiang Q, Chu J H, Xu X, Arslan I, Gage T E and Wen H 2023 *Nano Lett.* **23** 10213
[11] Kwon O H, Barwick B, Park H S, Baskin J S and Zewail A H 2008 *Nano Lett.* **8** 3557
[12] Baskin J S, Park H S and Zewail A H 2011 *Nano Lett.* **11** 2183
[13] Tong L, Yuan J, Zhang Z, Tang J and Wang Z 2023 *Nat. Nanotechnol.* **18** 145
[14] Sun S, Li Z, Li Z A, Xiao R, Zhang M, Tian H, Yang H and Li J 2018 *Nanoscale* **10** 7465
[15] Li Z, Sun S, Li Z A, Zhang M, Cao G, Tian H, Yang H and Li J 2017 *Nanoscale* **9** 13313
[16] Tanaka M and Tsuda K 2011 *J. Electron Microsc.* **60** S245
[17] Huang J, Kim M J, Chidambaram P R, Irwin R B, Jones P J, Weijtmans J W, Koontz E M, Wang Y G, Tang S and Wise R 2006 *Appl. Phys. Lett.* **89** 063114
[18] Jones E J, Azize M, Smith M J, Palacios T and Gradečak S 2012 *Appl. Phys. Lett.* **101** 113101
[19] Yurtsever A and Zewail A H 2009 *Science* **326** 708
[20] Yurtsever A, Schaefer S and Zewail A H 2012 *Nano Lett.* **12** 3772
[21] Flannigan D J, Cremons D R and Valley D T 2017 *J. Mater. Res.* **32** 239
[22] Feist A, Rubiano da Silva N, Liang W, Ropers C and Schäfer S 2018 *Struct. Dyn.* **5** 014302
[23] Bach N, Feist A, Möller M, Ropers C and Schäfer S 2022 *Struct. Dyn.* **9** 034301
[24] Nakamura A, Shimojima T and Ishizaka K 2022 *Faraday Discuss.* **237** 27

[25] Martin Y, Rouviere J, Zuo J and Favre-Nicolin V 2016 *Ultramicrosc.* **160** 64

[26] Morawiec A 2005 *Philos. Mag.* **85** 1611

[27] Carbone F, Baum P, Rudolf P and Zewail A H 2008 *Phys. Rev. Lett.* **100** 035501

[28] Maier H, Keller R, Renner H, Mughrabi H and Preston A 1996 *Philos. Mag. A* **74** 23

[29] Wittmann R, Kruse P, Frauenkron M and Gerthsen D 2000 *Philos. Mag. A* **80** 2215

[30] Zuo J M and Spence J C 2017 *Advanced Transmission Electron Microscopy* (New York: Springer)

[31] Feist A, Bach N, Rubiano da Silva N, Danz T, Möller M, Priebe K E, Domröse T, Gatzmann J G, Rost S, Schauss J, Strauch S, Bormann R, Sivis M, Schäfer S and Ropers C 2017 *Ultramicroscopy* **176** 63

[32] Houdellier F, Caruso G, Weber S, Hÿtch M, Gatel C and Arbouet A 2019 *Ultramicroscopy* **202** 26

[33] Zhu C, Zheng D, Wang H, Zhang M, Li Z, Sun S, Xu P, Tian H, Li Z, Yang H and Li J 2020 *Ultramicroscopy* **209** 112887

[34] Chang S L, Dwyer C, Barthel J, Boothroyd C B and Dunin-Borkowski R E 2016 *Ultramicroscopy* **161** 90

[35] Cattaneo M, Müller-Caspary K, Barthel J, MacArthur K E, Gauquelin N, Lipinska-Chwalek M, Verbeeck J, Allen L J and Dunin-Borkowski R E 2024 *Ultramicroscopy* **267** 114050